Piezoresistive Free-standing Microfiber Strain Sensor for High-resolution Battery Thickness Monitoring

Pariya Nazari,* Rainer Bäuerle, Johannes Zimmermann, Christian Melzer, Christopher Schwab, Anna Smith, Wolfgang Kowalsky, Jasmin Aghassi-Hagmann, Gerardo Hernandez-Sosa,* and Uli Lemmer*

Highly sensitive microfiber strain sensors are promising for the detection of mechanical deformations in applications where limited space is available. In particular for in situ battery thickness monitoring where high resolution and low detection limit are key requirements. Herein, the realization of a highly sensitive strain sensor for in situ lithium-ion (Li-ion) battery thickness monitoring is presented. The compliant fiber-shaped sensor is fabricated by an upscalable wet-spinning method employing a composite of microspherical core-shell conductive particles embedded in an elastomer. The electrical resistance of the sensor changes under applied strain, exhibiting a high strain sensitivity and extremely low strain detection limit of 0.00005 with high durability of 10 000 cycles. To demonstrate the accuracy and ease of applicability of this sensor, the real-time thickness change of a Li-ion battery pouch cell is monitored during the charge and discharge cycles. This work introduces a promising approach with the least material complexity for soft microfiber strain gauges.

1. Introduction

The state-of-the-art lithium-ion (Li-ion) battery is a widely used rechargeable energy storage device in application areas ranging from green electric mobility to all sorts of daily-life personal electronic gadgets. Increasing the lifetime of the Li-ion battery is of utmost importance, not only to prohibit premature capacity fade but also to effectively reduce the hazardous waste stemming from these devices. During the battery operation, several inevitable electrochemical reactions occur between the electrodes and the electrolyte due to Li-ion de/intercalation. On the one hand, lattice expansion, and contractions during charging and discharging, known as breathing cause reversible volume expansion, in the long run leading to gradual structural aging.[1] On the other hand, parasitic reactions such as lithium-plating, gas generation, and solid electrolyte interphase growth, decrease capacity retention over time and cause irreversible expansions known as swelling, leading to lithium inventory loss.[2,3] These reactions, depending on the used electrode and electrolyte chemistry cause relative volume changes ranging from 1% up to 10%.[3] Thus, in a battery management system, real-time monitoring of the volume changes

P. Nazari, G. Hernandez-Sosa, U. Lemmer
Light Technology Institute
Karlsruhe Institute of Technology
Engesserstrasse 13, 76131 Karlsruhe, Germany
E-mail: pariya.nazari@kit.edu; gerardo.sosa@kit.edu;
uli.lemmer@kit.edu

P. Nazari, R. Bäuerle
Institute of Organic Chemistry
Heidelberg University
Im Neuenheimer Feld 270, 69120 Heidelberg, Germany

P. Nazari, R. Bäuerle, J. Zimmermann, C. Melzer, W. Kowalsky,
G. Hernandez-Sosa, U. Lemmer
InnovationLab
Speyerer Str. 4, 69115 Heidelberg, Germany

R. Bäuerle, W. Kowalsky
Institute of High Frequency Technology
Technical University of Braunschweig
Universitätsplatz 2, 38106 Braunschweig, Germany

C. Schwab, A. Smith
Institute for Applied Materials
Karlsruhe Institute of Technology
Hermann-von-Helmholtz-Platz 1, 76344 Eggenstein-Leopoldshafen, Germany

J. Aghassi-Hagmann
Institute of Nanotechnology
Karlsruhe Institute of Technology
Hermann-von-Helmholtz-Platz 1, 76344 Eggenstein-Leopoldshafen, Germany

G. Hernandez-Sosa, U. Lemmer
Institute of Microstructure Technology
Karlsruhe Institute of Technology
Hermann-von-Helmholtz-Platz 1, 76344 Eggenstein-Leopoldshafen, Germany

of the Li-ion battery is a critical domain for improving its lifetime and performance.[4,5]

Battery health diagnostic through the characterization of volume or thickness changes has been investigated by numerous studies using different methods: neutron imaging,[6] in situ X-ray diffraction,[7,8] in situ atomic force microscopy,[9] 3D digital image correlation,[10,11] mechanical measurement methods,[1,2,12–15] thickness gauges,[3,16] ultrasonic probing,[17,18] and optical sensors.[19–22] However, all the measurement methods and sensors either require complicated laboratory setups, cannot be seamlessly integrated for in situ monitoring, and are not cost-efficient.[4,23] Therefore, there is a critical demand for all-round volume monitoring approaches that deliver high-precision data and provide low-cost and facile integration to a wide variety of battery forms.

Piezoresistive stretchable polymer composites (PSPC) have been investigated as easy-to-tailor stretchable strain sensors for applications in electronic skins,[24,25] integrated soft robotics,[26] and wearable electronics.[27,28] Among all literature reports, freestanding fiber-shaped PSPC-based strain sensors provide miniaturized shape and conformability to dynamic surfaces as well as high performance.[29] Despite these promising properties, their use in the field of battery expansion monitoring has been left unexplored. Typically, fiber-shaped PSPC strain sensors comprise a network of a conductive filler (e.g., carbon black,[30] silver nanowire,[31] or a hybrid combination of different particles[32,33]), embedded in an elastic polymer (e.g., polydimethylsiloxane,[34] thermoplastic polyurethane[35]). Upon applied strain, the induced mechanical deformation translates to an alteration of the conductive paths which are created by conductive fillers, and thus a change in electrical resistance is obtained. The reported fiber-based sensors demonstrate the smallest strain detectable in low-strain ranges of $\geq$ 0.01%.[30,36–38] However, for most typical Li-ion battery expansion monitoring, a strain detection with an accuracy below 1 μm dimension change is required, which has not been achieved so far.[1,8,14,20]

In this work, we implemented an innovative strategy to realize a microfiber-based strain sensor for battery expansion monitoring. We utilized silver-coated glass microspheres as conductive fillers in an ethylene-vinyl-acetate copolymer (EVA) matrix to obtain freestanding stretchable conductive microfiber via the upscalable wet-spinning method. Implementing spherical-shaped fillers yielded sensors exhibiting a linear response from a remarkably low strain of 0.005% up to 14%. Our microfiber provides an outstanding high resolution in detection of 1 μm displacement along its length. To the best of our knowledge, the smallest strain detectable in this work is the lowest reported in piezoresistive strain sensors. The microfiber sensor showed no deterioration of electrical response after 10 000 strain-release cycles (at 1% strain). Finally, we demonstrate for the first time the utilization of conductive microsphere-based fibers for the high-precision real-time detection of thickness changes in a Li-ion pouch cell during charging and discharging cycles.

2. Results and Discussion

As illustrated in **Figure 1**a, the wet-spinning method is used for the fabrication of the stretchable microfiber strain sensors. In a wet-spinning approach,[32,38] a solution mixture is extruded via a spinneret nozzle into a non-solvent coagulation bath. Here we use ethylene-vinyl-acetate copolymer (EVA) as an elastic polymer to house the conductive fillers. We chose anisole as a favorable green and nontoxic solvent for dissolving the EVA, and acetone as an appropriate non-solvent. These solvents are chosen based on the analysis of the Hildebrand-Hansen solubility parameters and the relative energy differences with EVA (Note S1 and Table S1, Supporting Information).[39,40]

During the extrusion of the solution mixture into the coagulation bath, the counter diffusion between anisole and acetone molecules takes place (Figure 1a right) due to the net gradient concentration.[41,42] Anisole molecules are removed from the EVA solution diffusing outward into the coagulation bath and the acetone molecules diffuse inwardly, yielding decreased solubility of EVA. As a result of this solvent exchange, the polymer starts to densify, first at the periphery of the interface where it is in closest contact with the coagulation bath, forming a gel-boundary layer.[43] The boundary moves inwardly in a homogenous way during the coagulation time, and finally reaches the center of the microfiber when all the available EVA is densified. Thus, EVA condenses from the viscous solution into a fiber shape aided by the shear force exerted by the nozzle. In our experiment, the nozzle is moved along a circular path in the coagulation bath to exert an additional shear-drawing force from the non-solvent to the spinning solution (Video S1, Supporting Information). These two forces,[44,45] give rise to a compact, uniform, and cylindrical-shaped long microfiber (Figure S1, Supporting Information). To allow for complete polymer densification and solvent exchange, the extruded microfiber is kept in the non-solvent bath for 3 minutes. After coagulation, the formed free-standing microfiber is pulled out of the acetone bath and collected using a spool as shown in Figure 1b. Then to ensure the removal of the residual acetone in the microfiber, it is dried at room temperature under a vacuum. This facile method is fully scalable for the high-throughput fabrication of microfiber strain sensors. Further, Figure 1c demonstrates that the developed microfiber sensor can conform to arbitrarily curved surfaces highlighting its potential use in various battery form factors (e.g., pouch cells, cylindrical, etc.). As shown in the optical microscope image in Figure 1d, the dried microfiber has a cylindrical shape with a diameter of 330 μm ±10 μm. The diameter of the microfiber can be controlled by the wet-spinning parameters (Figure S2, Supporting Information). Figure 1e depicts a prepared microfiber strain sensor with electrodes attached at the two ends. The schematic drawing in Figure 1f shows how the conductive silver-shell/glass-core microspheres embedded in EVA form electrically conductive percolative paths with a small contact interface. The microstructure of the lightweight microfiber (0.133 mg mm^{-1}) is studied by scanning electron microscopy (SEM). The top and cross-section views illustrate the compactness of the microfiber (Figure 1g). The percolated network of conductive microspheres (average diameter of $\approx$ 4 μm) within the EVA matrix is visible in Figure 1h. The high-magnification cross-section images of the microfiber in Figure 1i and Figure S3 (Supporting Information) show the nanoscale features of the silver shell coating (50 – 80 nm) on the spherical glass core. The percolation threshold of our microsphere-EVA microfibers is estimated to
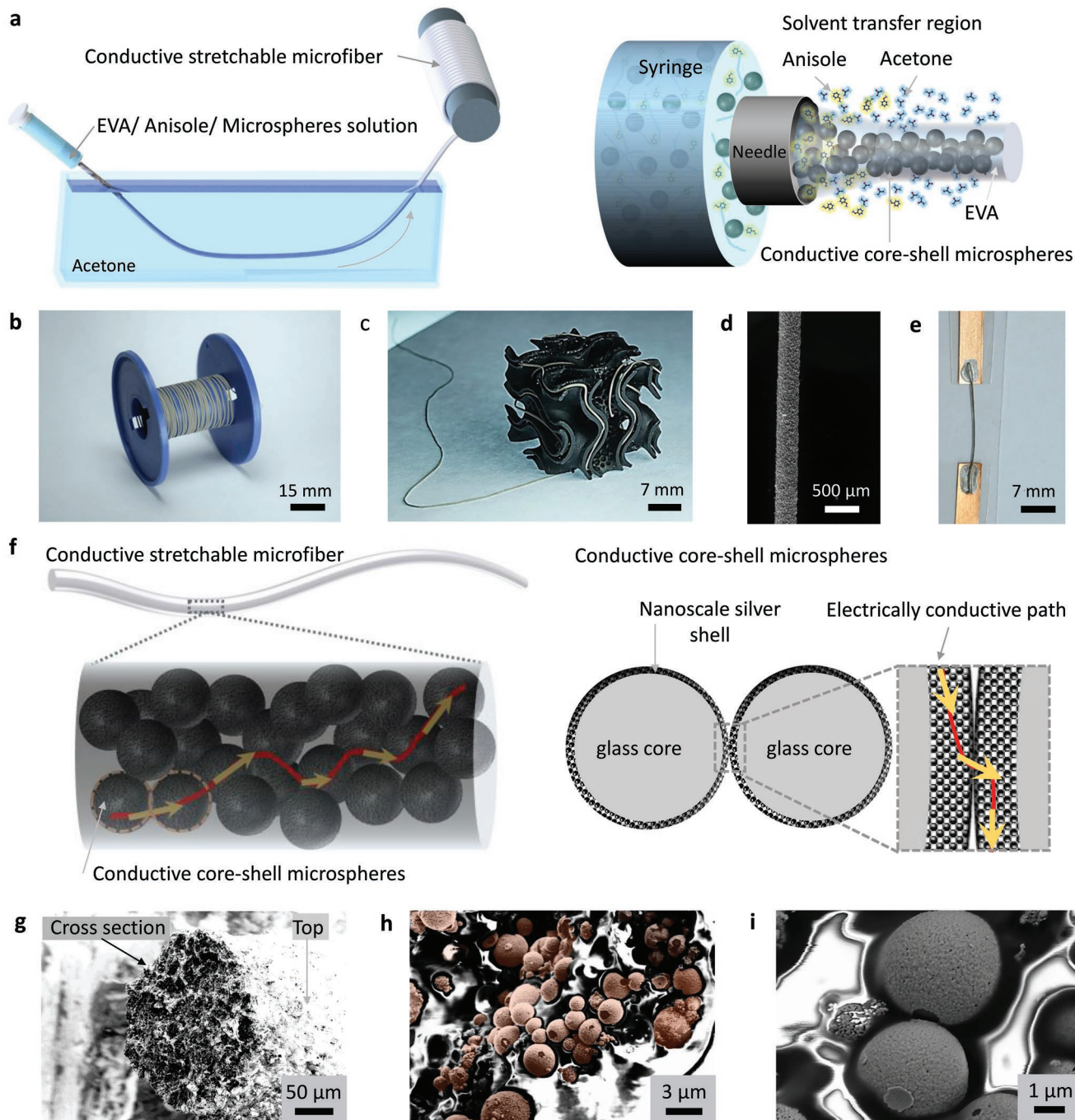
Figure 1. Fabrication and structure of a free-standing stretchable microfiber strain sensor. a) Schematic illustration of the fabrication method of microfiber from a solution mixture including conductive core-shell microspheres and a copolymer elastomer. b) Photograph of the fabricated microfiber collected on a spool. c) Photograph of the microfiber conformed around and into a 3D printed structure with curved features. d) Optical microscope image of the microfiber. e) Photograph of the microfiber strain sensor and the attached electrodes. f) Schematic illustration of the microfiber. Applying strain to the conductive microfiber decreases microsphere interconnections in the matrix, and reduces the conductive paths, resulting in increased resistance. g) Cross-section SEM image of the microfiber. h) Magnified SEM cross-section image with digitally colored conductive core-shell microspheres. i) SEM image of microspheres with nanoscale silver shell.

be 13 vol.% (Note S2 and Figure S4, Supporting Information). To ensure a stable and repeatable electrical response, we chose the 20 vol.% to fabricate the microfiber sensors. It is important to note that by using a nanoscale thin conductive shell on a microscale insulating spherical core, we have a significantly low volumetric ratio (≈1.9 vol.%) of the conductive part to the total volume of sensor material (elastomer, glass cores, and spherical silver shell).
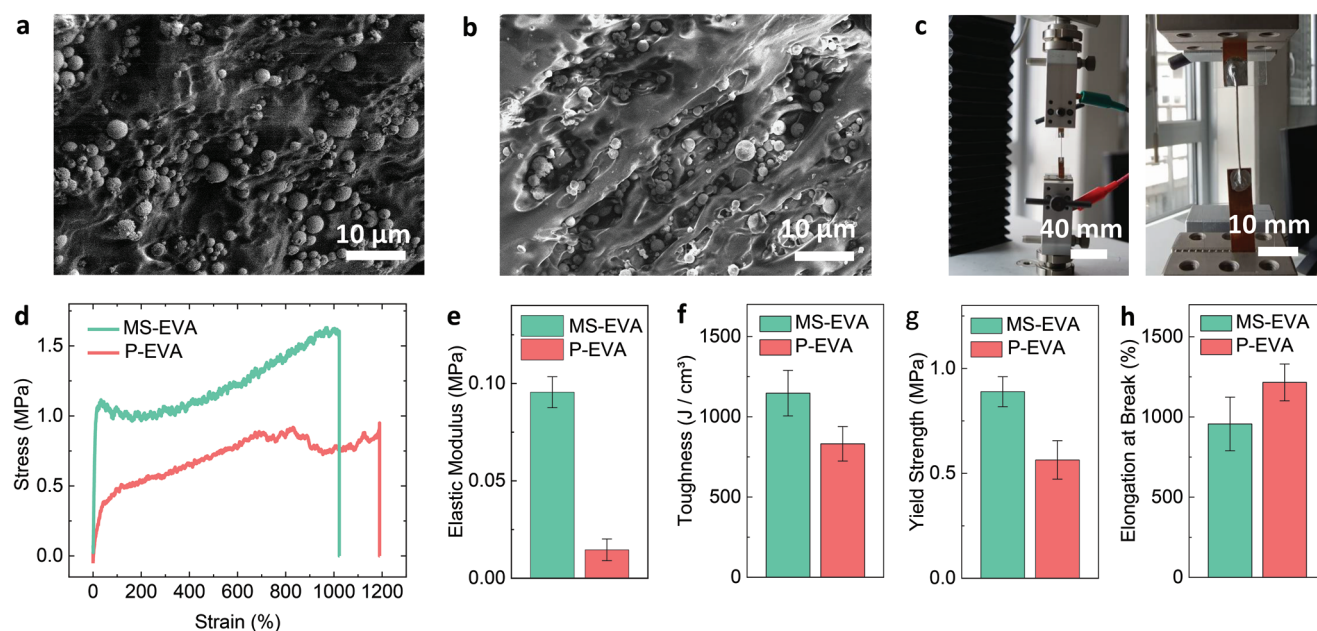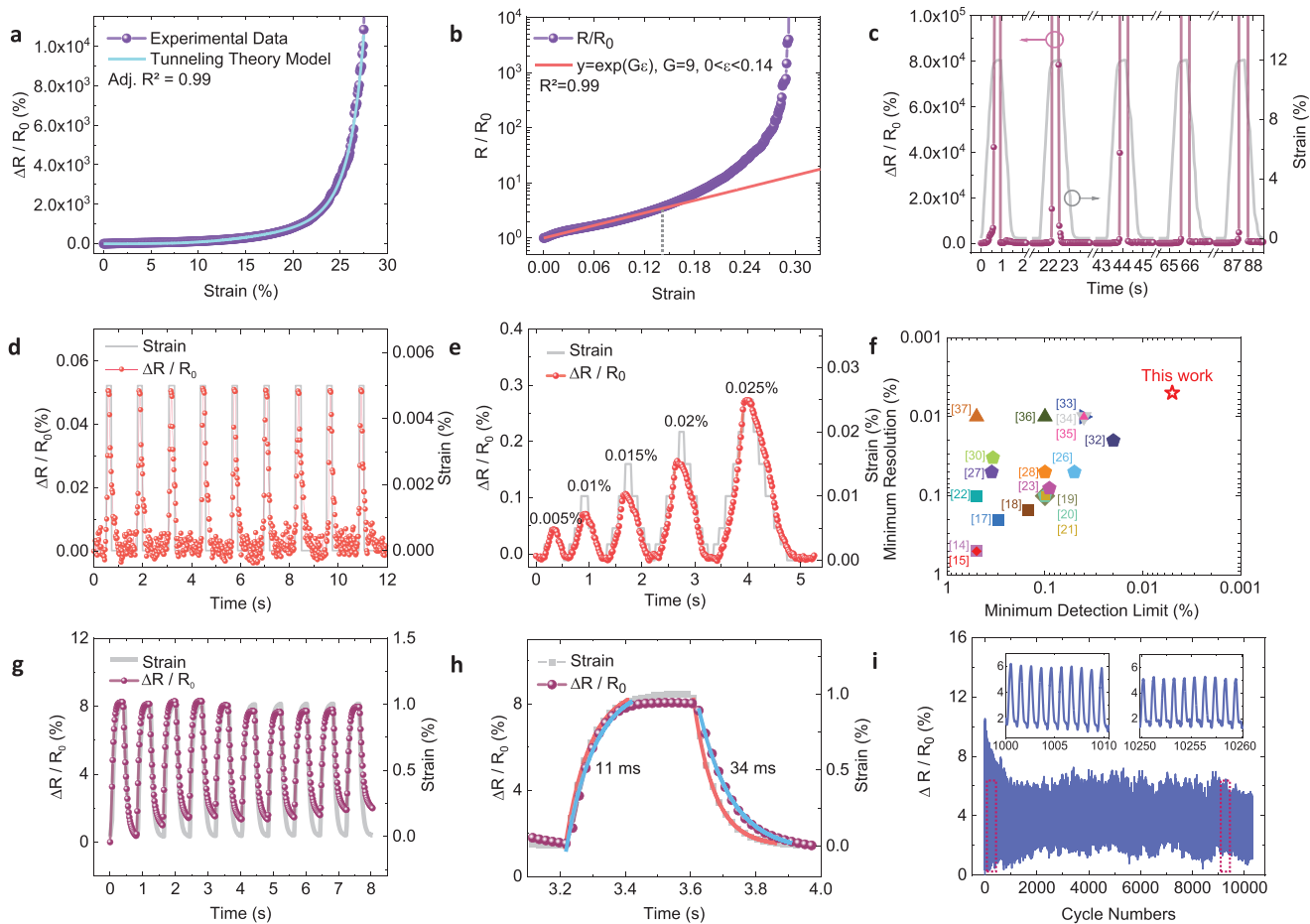
Figure 2. Mechanical properties of the microfibers. a) Longitudinal SEM cross-section image of the microfiber before application of tensile strain. b) Longitudinal SEM cross-section image of the microfiber under a tensile strain of 70%. c) Photographs of the microfiber under electromechanical tests (left: overview, right: detailed view). d) The engineering stress versus strain response of a microsphere containing microfiber (MS-EVA) and a pristine elastic polymer microfiber (P-EVA) (strain rate is 100 mm min⁻¹). Bar plots of the mechanical parameters of the MS-EVA and P-EVA: e) Elastic modulus, f) Toughness, g) Yield strength, h) Elongation at break.

The electromechanical performance of the microfiber is closely dependent on how the solid conductive core-shell microsphere presence in the elastomer matrix impacts its mechanical properties. Here, EVA copolymer with physically cross-linked ethylene and vinyl acetate chains is chosen as a cost-effective and beneficial elastomer (Figure S5, Supporting Information). A closer look at the interface of the EVA and the microspheres in **Figure 2**a and under tensile strain in Figure 2b and Figure S6 (Supporting Information) illustrates that a weakly bonded blanket-like layer is formed around the microspheres. Since EVA is already polymerized, it is assumed that its mobile amorphous vinyl acetate chains and semi-crystalline ethylene chains cannot form strong bonds to the surface of the microspheres. The loose interfaces are ascribed to stem from the weak Van-der-Waals forces between the polar chains of the vinyl acetate and the silver shell of the microspheres. This observation further suggests that EVA facilitates the agglomeration of a percolated network of conductive fillers and allows for the formation of electrically conductive paths at low percolation ratios.[46]

The mechanical properties of the microfibers are studied by an external uniaxial tensile strain (Figure 2c and Figure S7, Supporting Information). The engineering stress versus tensile strain evolution of pristine elastomer microfibers (P-EVA) is compared with microfiber sensors containing conductive core-shell microspheres (MS-EVA) as presented in Figure 2d and Figure S8. The parameters obtained by their mechanical responses are summarized in Figure 2e–h, Figure S9, and Table S2 (Supporting Information). P-EVA shows a low elastic modulus of 14 KPa ± 4 KPa, while MS-EVA yields 95 KPa ± 8 KPa (Figure 2e). The low elastic modulus of P-EVA is attributed to the presence of the bulky acetoxy group preventing the adjacent ethylene chains from crystallizations, hence EVA has an amorphous and rubbery nature.[47,48] With the inclusion of microspheres, the elastic modulus of microfiber is increased. The increase in elastic modulus and the subsequent increase in toughness of the MS-EVA, as demonstrated in Figure 2f, is ascribed to the polymer-toughening effect which is caused by the embedding of microspherical fillers into an elastomer.[49] This phenomenon is assumed to stem from the reduction in amorphous (vinyl-acetate) polymer chain mobility in the EVA matrix when solid microspherical fillers are used. It is important to note that even after toughening, the elastic modulus of MS-EVA remains sufficiently low for sensing small strain. Thus, this strain-sensing concept is a promising candidate with high conformity for small strain-sensing applications.[50] The relatively low elastic modulus of the MS-EVA as compared to other fillers is explained by the spherical shape, as such there is a minimal number of contact points between fillers, resulting in low internal friction.[38] The corresponding increase in yield strength of MS-EVA compared to P-EVA is shown in Figure 2g. Additionally, the strain after which the microfiber exhibits a plastic deformation (i.e., the mechanical yield strain) decreases from ≈89% for P-EVA down to ≈28% for MS-EVA (Figure S9, Supporting Information). As demonstrated in Figure 2h, P-EVA shows an elongation-at-break of ≈1282%, due to the high stretchability of the EVA elastomer. The inclusion of microscale conductive fillers reduces the elongation at the break to ≈956% for MS-EVA. This shortened elongation at break can be attributed to the increased microstructure breakdown in the framework of amorphous (vinyl acetate) and semi-crystalline (ethylene) EVA copolymer due to the presence of the microspheres. In MS-EVA, the physical bonds of the polymer at the interface of fillers and the EVA matrix, and the chains linking the fillers, rupture at lower strains. Whereas, in the

2212189 (4 of 11)

Figure 3. Strain sensing properties of the microfiber sensor. The initial length of the microfiber sensor is 20 mm, and the strain rate is 100 mm min^{-1} or the equivalent of 8.3% s^{-1} unless otherwise specified. a) Relative change of resistance of the microfiber as a function of applied tensile strain (data points) and fit based on tunneling theory (light blue line) (for more information, see Note S3 and Table S3, Supporting Information). b) Relative change of resistance of the microfiber versus strain. At the linear response region of the microfiber ($\varepsilon \leq 14\%$), leading to a working factor of 0.14, a strain sensitivity (G) of 9 is obtained via fitting ($R^2 = 0.99$). c) Retrieving conductivity after complete electrical disconnection under the cyclic tensile strain of 12% at a fast strain rate of 900 mm min^{-1} (the equivalent of 75% s^{-1}). d) Relative change of resistance under a cyclic tensile strain of 0.005% showing the minimum detection limit of the microfiber sensor with a signal-to-noise ratio of 5. e) Strain sensing resolution of the microfiber sensor under a stepwise increase of tensile strain in the low-strain regime. f) Comparison of minimum strain detection limit and minimum resolution in strain detection of the microfiber sensor in this work and the reported strain sensors (see Table S5, Supporting Information). g) Reproducibility of the microfiber responses under a fast cyclic tensile strain of 1% ($\dot{\varepsilon} = 900$ mm min^{-1}). h) Response time evaluation under the application of 1% tensile strain ($\dot{\varepsilon} = 900$ mm min^{-1}, for more information, see Note S4, Supporting Information). The numbers in the panel give the differences in the rise and fall times of the sensor compared to the applied strain. i) Durability of the microfiber response over >10 000 cyclic tensile strain of 1%. Insets show the enlarged microfiber responses at two temporal windows of 1000 to 1010th cycles (left), and 10 250 to 10 260th cycles (right).

case of a P-EVA upon the same strain that could cause total failure at MS-EVA, the chains might disentangle and rearrange preventing the over-stretching of shorter chains.[51] Thus, the P-EVA is observed to accommodate larger strains than MS-EVA and can be torn at a larger strain.

The electromechanical response of the microfiber sensor is further investigated by applying a linearly increasing tensile strain (ε) until complete electrical disconnection. The relative change of resistance of the sensor, defined as $\Delta R/R_0$, is shown in **Figure 3**a. Here, $\Delta R = R - R_0$, R representing the resistance at the applied strain, and R_0 the initial resistance of the microfiber. To describe the observed piezoresistive response, we utilized a standard model based on tunneling theory applicable to a percolative network of conductive fillers in an insulating elastomer

(Note S3, Supporting Information).[27,52] Based on this model, the $\Delta R/R_0$ can be formulated as presented in Equation (1). Figure 3a shows that the measured $\Delta R/R_0$ is in good agreement with the tunneling theory model. The fitting parameters to Equation (1) are listed in Table S3 (Supporting Information).

$$\frac{\Delta R}{R_0} = (1 + E\varepsilon) \exp\left[(A + FE)\varepsilon + B\varepsilon^2 + C\varepsilon^3 + D\varepsilon^4\right] - 1 \tag{1}$$

As an indication of the strain sensitivity, the gauge factor (GF) as a key figure of merit is usually defined as GF = $\Delta R/R_0 \cdot 1/\Delta\varepsilon$. But this is only applicable in the low strain regime where the sensor cross-section and its length are not significantly changed (an important point mostly misinterpreted

in the literature).[50,53] Since the piezoresistive response has an exponential nature, the more practical strain sensitivity (G) can be defined as described in Equation (2).[53]

$$\frac{R}{R_0} = \exp(G\varepsilon) \tag{2}$$

As a crucial requirement for the reliable application of a PSPC-based strain sensor, their response should be calibratable throughout the sensing range. As discussed by Boland et. al.,[50,54,55] in response to the applied strain, the resistance of a PSPC-based sensor follows a two-phase trend. In the low-strain region, the behavior is governed by an exponential increase of relative change of resistance leading to a linear dependence in a semilogarithmic plot. The exponential describes the behavior well until reaching a specific point in strain, i.e., the working factor. After this point, it is assumed that the effect of higher orders of the strain appears, thus the R/R_0 response becomes non-linear. After reaching the working factor, the further increment of applied strain leads to an increase in tunneling distance (i.e., interparticle distance), significantly increasing the rate of resistance change.

For practical applications though, the non-linear region is not reliable, mainly due to possible electromechanical hysteresis stemming from the inherent viscoelastic properties of the utilized elastomer material.[50] Figure 3b, demonstrates R/R_0 as a function of applied strain. In the linear R/R_0 range, the corresponding strain sensitivity G of 9 ± 0.02 ($R^2 = 0.99$) is obtained by fitting Equation (2) to the R/R_0-versus-strain data. Thus, the gauge factor GF for a small strain range also amounts to 9. The working factor as another figure of merit that can be used for classifying the response range of the developed microfiber sensors[50] is estimated to be 0.14. In this range, the linear R/R_0 versus-strain facilitates calibration of the sensor response. As presented in Figure S10, and Table S4 (Supporting Information), the mean strain sensitivity of 10 microfibers over their linear-response range is 9.1 ± 1.7, and the mean working factor is 0.139 ± 0.029. We note that, as shown in Figure S11 (Supporting Information), using 35 μm microspheres (average size), a strain sensitivity of 24 is obtained. However, the increased strain sensitivity compared to the 4 μm microspheres microfiber is achieved at the cost of reduced working factor and stretchability. Employing 35 μm microspheres, a lower working factor of 0.008 and a maximum electromechanically responsive stretchability of up to 1% is obtained. On the one hand, the sensitivity of commercially available thin film strain gauges is low (GF ≤ 2), and they typically have limited stretchability (< 5%).[1,56] On the other hand, the reported works on stretchable microfiber-based piezoresistive strain sensors responsive to small strains (ε < 1%) often employ a multitude of different materials,[30,44,57] or costly and tedious fabrication procedures are involved (for example high vacuum, high temperature, or hazardous chemicals).[27,44,58] It is important to note that in our work the high strain sensitivity is obtained by using only one type of conductive filler and one type of elastic polymer in a facile method.

Figure 3c depicts the $\Delta R/R_0$ of one microfiber under a cyclic strain of 12%, carried out at a high strain rate of 900 mm min^{-1}. At the peak of strain, the microfiber gets electrically disconnected ($R_{\varepsilon max} > 10^9$ Ohm). Notably though, when strain is removed, the conductivity of the sensor is reversibly restored ($R_{\varepsilon = 0} < 55$ Ohm). Based on this observation we assume that, when the microfiber is brought back to the relaxed state, the interrupted conductive paths are -to a large extent- reconstructed. The reconstruction of conductive paths is associated with the effective design of our sensor using spherical fillers in combination with the beneficial properties of the EVA matrix. Due to the high elasticity of EVA, its favorable interface with the microspheres, and the inherently low friction of spherical surfaces, our microfibers are capable of efficiently recreating conductive paths. Further, we observed that the threshold of maximum reversible conductive stretchability can be increased to 25% when a slower strain rate of 100 mm min^{-1} is applied (Figure S12, Supporting Information). This rate-dependent conductivity restoration can be largely attributed to the increase in filler network breakdown under higher strain rates, an effect known as the Payne effect in filled elastomers.[54] It is noteworthy, that without the need for further encapsulation materials or reinforcement methods, which is an established method in restoring the conductivity elsewhere,[44,59] our sensor demonstrates robustness to strains higher than its working factor. We nevertheless observed electromechanical hysteresis in $R_{\varepsilon = 0}$ (Figure S13, Supporting Information) due to the viscoelasticity of the EVA as well as increased microstructure breakdown and possible formation of voids at the interface with EVA[49] (Figure 2b). The irreversible electrical disconnection is reached above the mechanical yield strain of the MS-EVA (ε >28%), presumably due to a surge in the number of polymer chain ruptures and void formation. Subsequently, the number of electrically disconnected paths surpasses that of recreated conductive paths.

The detection limit (the smallest strain detectable) of the microfiber is investigated through a sequential cyclic strain test. As presented in Figure 3d, upon application of a very small strain of 0.005%, the microfiber sensor exhibited a highly repeatable $\Delta R/R_0$ of 0.05%. From this $\Delta R/R_0$, we estimate a signal-to-noise ratio of five, providing an easily detectable output signal for very small strain sensing applications. This detection limit corresponds to distinguishing a 1 μm length change over the total microfiber sensing length of 20 mm. This demonstrates the extremely high sensitivity of our sensor in this deformation range.

Furthermore, the capability to resolve very small strain values is also a crucial property for strain sensing applications. Figure 3e shows the obtained response when subjecting the sensor to sequentially increasing strain from 0.005% to 0.025%. In this low-strain regime, we were able to differentiate the corresponding $\Delta R/R_0$ with remarkably high precision within strain steps of 0.005%. This step size corresponds to a deformation of 1 μm. To engineer this detection limit and resolution for small strain sensing applications, we chose spherical-shaped conductive particles.[38] This approach effectively minimizes the interface area (the total number of interparticle contact points). Correspondingly, under the slightest strain, the number of interparticle connections decreases thus increasing the resistance of the microfiber. As depicted in Figure 3f, the reported detection limit, and resolution in our work are the lowest among piezoresistive strain sensors in the literature (Table S5, Supporting Information).

In Figure 3g, we examine the reproducibility of the microfiber response to a cyclic strain of 1% applied at a high rate of 900 mm min^{-1}. The obtained $\Delta R/R_0$ during the test reversibly mirrored the course of applied strain with minimal hysteresis. The response time of the microfiber is considered as the time difference between the time it takes for exerting the strain, or to release it, compared to the time it takes for the microfiber to respond to the applied or released strain (Note S4, Supporting Information). As shown in Figure 3h, the difference in response time to the applied cyclic strain of 1% is estimated to be 11 ms, and 34 ms for the stretching and relaxing stages respectively. Figure S14 and Table S6 (Supporting Information) depict the statistical data of the response time of 10 microfibers against applying and releasing a strain of 1%. A longer delay in the relaxing phase can be ascribed to a partial reduction of conductive paths and the typical time-dependent viscoelastic response of a rubbery elastomer.[60] The observed fast response of the microfiber sensor in this work enables the real-time monitoring of applied strain in a variety of applications. For these applications, reproducibility and durability of the response over a large number of cycles are of high importance. As depicted in Figure 3i, the microfiber shows a stable response under a strain range of 0–1% for >10 000 cycles. The initial reduction in $\Delta R/R_0$-versus-strain within the first ≈900 cycles can be attributed to the Mullins effect, a typical stress relaxation mechanism, as one implication of stress softening characteristics in elastomers under mechanical cycling.[51,54,61] However, a reproducible $\Delta R/R_0$ of ≈5% is observed throughout the measurement (see insets of Figure 3i) highlighting the robustness and reliability of the microfiber strain sensor. We also demonstrated the long-term stability of several sensors by measuring their static resistance in one-month intervals within 12 months (Figure S15, Supporting Information).

Overall, the free-standing microfiber strain sensor presented in this work exhibits a very small strain detection limit, high resolution, linearity, and lightweight. Furthermore, it showed a fast reaction time and durability over 10 000 cycles. Therefore, this sensor is a promising candidate for applications where priority is given to the real-time detection of small strains with a high signal-to-noise ratio.

2.1. Microfiber Strain Sensors in Battery Thickness Monitoring

As previously discussed, Li-ion battery health can be monitored by measuring and analyzing the change in its thickness during charge and discharge cycles. The choice and implementation of a suitable strain sensor highly depend on the requirements of the battery under investigation (e.g., geometry, available space, etc.). The outstanding properties and flexible design of our microfiber strain sensor suggest it is well suited to address the current challenges in the real-time thickness evolution of Li-ion batteries.

As shown in **Figure 4**a–d, we constrained a rectangular Li-ion pouch cell fabricated in our laboratory between two larger plates on its upper and lower sides to record its thickness evolution during cycling. The thickness monitoring in the z-direction (Δz) is enabled by seven microfiber-based strain sensors positioned vertically on three sides of the plates and one side is allocated for the battery electrode connections. The

real-time two-probe resistance changes of all seven microfibers with an active sensing length of 7.3 mm (Figure 4b) are simultaneously monitored using a source measure unit. As shown in Figures 4a,c, four springs are used to keep the plates in contact with the surface of the cell throughout the measurements. They apply a small force and provide a more uniform z-direction displacement of the upper plate. As a reference, a commercial displacement monitoring sensor (RDS) is used at the geometrical middle point of the cell (Figure 4c; Figure S16, Supporting Information). Figure 4d depicts a schematic of the Li-ion cell configuration examined in this study and its stack cross-section (for more information see the Experimental Section). Figure 4e shows the Li-ion cell voltage during one representative charge and discharge cycle, the readings of the RDS, and that of one microfiber. First, cell charging is performed up to 4.2 V with constant current (CC) and continued with constant voltage (CV) with a 1C rate. Then, discharging to 3 V is done with a CC mode with a 1C rate. In Figure 4f the dynamic $\Delta R/R_0$ of the seven microfiber sensors (f1–f7) monitoring the corresponding cycle is shown. Following the data of the reference sensor, the microfiber signals provide interesting information on the expansion phases in Li-ion cell cycling. During charging in the CC phase, the cell is expanded, reaching a maximum thickness increase of 62 µm (based on RDS data, which is measured at the center). The displacement experienced by microfiber f7, located at the edge, is calculated by plugging its corresponding resistance response and the strain sensitivity (G) of 9 into $R/R_0 = \exp(G\varepsilon)$. We estimated that at the peak of cell expansion, f7 experienced an elongation of 80 µm. It is noteworthy that the slight difference in the measured displacements can stem from the difference in positions of the RDS compared to the microfibers (Figure S17, Supporting Information). The cell expansion during this phase applied a tensile strain to the microfibers reaching 0.85% at the peak, resulting in a high $\Delta R/R_0$ of ≈10%. Notably, cell shrinkage starts while still charging in the CV phase rather than the expected start of discharge. The $\Delta R/R_0$ shapes at the beginning of the CV phase clearly reflect this phenomenon, e.g., f7 shows an $\Delta R/R_0$ of 10.8% at the end of CC charging and then reduces to 9.7% at the end of CV charging. This shrinkage corresponds to a $\Delta\varepsilon$ of -0.05%. This observation leads to the assumption that in the CV phase, while reducing current, volume relaxation is stronger than the volume expansion by lithiation of the anode. Furthermore, discharging with CC mode shows thickness contraction back to its initial status. Figure 4g shows the $\Delta R/R_0$ of three sensors over four consecutive cycles compared with the RDS data. We observed that all sensors closely follow the reference measurement with high accuracy and reproducibility. Overall, a decrease in maximum expansion over time is observed, as reflected in microfiber responses and RDS readings with third and fourth cycles showing almost identical expansion behavior. One side note is that the thickness change monitored by the RDS unit is performed at the center of the cell. As shown in Figure S18 and Table S7 (Supporting Information), independent static thickness measurements at different positions on top of the cell originally show inhomogeneous expansion most likely due to the cell manufacturing process and pouch foil influences. The slight pressure applied by springs on the four corners of the plate holding the pouch cell, balances and distributes these

**ADVANCED
SCIENCE NEWS**

www.advancedsciencenews.com

**ADVANCED
MATERIALS**

www.advmat.de
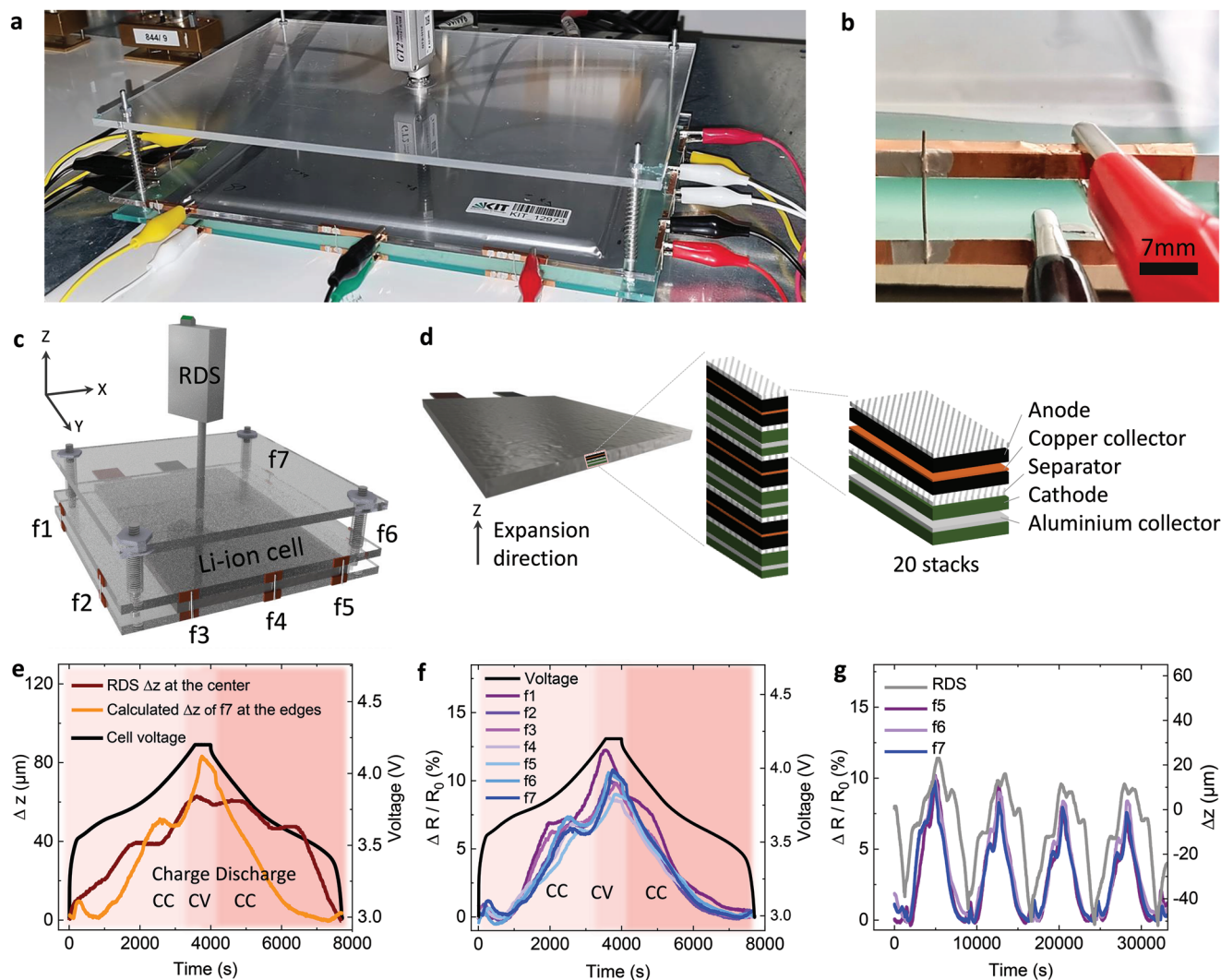
Figure 4. Employing microfiber sensors for Li-ion cell thickness monitoring. a) Photograph of the battery thickness monitoring setup (see also Figure S16, Supporting Information). It is comprised of a Li-ion pouch cell held between two plates. On top of the cell, the third plate is set to have a reference displacement sensor positioned at the center. This sensor is connected to a computer, and an array of our microfiber sensors is attached on three sides of the setup. b) Closeup of one microfiber strain sensor at the side of the setup. The two plates sandwiching the Li-ion cell are kept in contact with the cell by springs in the corners. c) Schematic of the setup for battery thickness monitoring. The thickness change of the cell is measured along the *z*-direction. The response of the microfiber strain sensors f1–f7 is collected at the sides using a multichannel source measure unit. d) Schematic of the Li-ion pouch cell, its expansion direction, the cell configuration inside the pouch, and the sequence of the layers. e) The thickness profile of the Li-ion cell along the z direction monitored at the center by the reference sensor during one charge and discharge cycle, the calculated displacement experienced by one microfiber at the edge of the cell, and cell voltage versus time during the same cycle. f) Resistance change profile of f1–f7 microfiber sensors during one charge and discharge cycle as a result of tensile strain induced by thickness expansion, and the Li-ion cell voltage-versus-time during the same cycle. g) Relative resistance change profile of three microfiber strain sensors as a result of applied strain during four consecutive charge and discharge cycles.

point-to-point differences in thickness to most parts. We note that the signals of our low-cost and integrable microfiber strain sensors are in full agreement with the RDS signals taken with a dedicated instrument. All stages of the expansion and contraction dynamics are accurately resolved with easily detectable resistance changes. Furthermore, the maximum volume expansion of most commercial Li-ion pouch cells is >1%.[62–65] Therefore, our microfiber sensors can be applied to monitor the volume expansion of commercial Li-ion cells.

The introduced microfiber sensor in this work demonstrates the simplicity and accuracy of the proposed strain sensing

mechanism for reliable Li-ion battery expansion monitoring, providing high-resolution data for battery management systems. In addition to reversible expansions, irreversible expansions (due to, e.g., aging effects)[2] that can detrimentally cause a cell explosion or leakage can be potentially monitored by the developed microfiber strain sensor. Furthermore, based on the dynamic responses of our microfiber in addition to its durability against >10 000 strain cycles, it can be concluded that in situ volume monitoring of a Li-ion battery over its entire lifetime is feasible based on integrated networks of microfiber sensors inside the battery pack.

3. Conclusion

In summary, we successfully demonstrated high-resolution real-time thickness monitoring of a Li-ion battery by employing a highly compliant microfiber-based sensor. The high resolution in low-strain detection was achieved by employing microspherical core-shell conductive fillers as the sensing elements embedded in an elastomer. This approach renders a highly linear response and high sensitivity in the working range as well as a fast response time. The promising dynamic strain sensing properties, lightweight, miniature form factor, in addition to durability over 10 000 cycles suggest that this economic and simple approach offers promising pathways for in situ Li-ion battery thickness monitoring applications. Furthermore, a microfiber sensor based on microspherical fillers unlocks a new pathway toward realizing reliable high-resolution strain detection for other small strain sensing applications. Their application can be expanded to other areas that require high-resolution strain sensing with a non-invasive approach in a limited available space.

4. Experimental Section

Materials: Ethylene vinyl acetate copolymer resin with 40 wt.% vinyl acetate (ELVAX 40 W) was purchased from DuPont de Nemours, Inc. Conductive core-shell silver coated soda lime glass microspheres (SLGMS-AG-3.3 1–7 um – 10 g) were purchased from Cospheric LLC. Anisole (anhydrous, 99.7%) and acetone (ACS reagent, 99.5%) were obtained by Sigma Aldrich. The materials were used as received.

Preparation of the Polymer Solution: The optimized EVA solution was prepared by mixing EVA copolymer resins having 40 wt.% vinyl acetate with anisole in a 1:4 weight ratio. This solution mixture was stirred at 55 °C for 3 h to ensure the homogeneous dissolving of EVA in anisole. Then the prepared solution was kept at room temperature for 15 min to reach room temperature before microsphere filler intermixing.

Preparation of the Spinning Solution: For the preparation of the spinning solution, a solid powder of conductive core-shell microspheres was added to the prepared polymer solution with 20 vol.% at room temperature by mechanical mixing for 30 s. The prepared spinning solution was used immediately after mixing.

Wet Spinning of the Microfibers: For the fabrication of conductive microfibers, the prepared spinning solution was loaded into a 3 mL syringe and spun into a nonsolvent bath of acetone, at room temperature. The optimized wet spinning rate of 50 mm s^{-1} was chosen with a needle gauge of 18 and needle length of 25 mm. The solution was dispensed in the nonsolvent bath using a dispenser pump (Martin Smart Dispense 06). To allow for complete coagulation of the ≈2 m long dispensed microfiber, it was kept in the acetone bath for 3 min right after dispensing. Subsequently, the formed microfiber was collected using a 20 mm DIA 3D printed spool. Then to evaporate the residual acetone in the microfiber, it was dried at room temperature under a 100 mbar vacuum for 1 h.

Preparation of the Microfiber Strain Sensors for Mechanical and Electrical Characterizations: For the mechanical and electrical characterizations, the dried microfiber was cut into ≈25 mm pieces (20 mm active sensing length, and an excess of ≈5 mm for electrode connections). Thereafter, contact electrodes at the two microfiber tails were adhered on a pre-cleaned 5 mm wide copper tape using silver lacquer. The silver lacquer was left to dry at room temperature for 10 min before mechanical and electrical characterizations of the microfibers.

Characterizations of the Microfiber Strain Sensors: Field emission scanning electron microscopy (SEM) top-view and cross-sectional images of the microfibers were taken with a ZEISS Supra 60VP scanning electron microscope. For the cross-sectional imaging, the microfiber was cooled down using liquid nitrogen and broken. The micrograph images were taken using a Nikon Eclipse 80i microscope. For the mechanical and electrical characterizations, the prepared microfibers with an active initial sensing length of 20 mm were strained by an Alluris Universal Test Instrument FMT-310BU with a 50 N force and displacement transducer head (FMT-310FUC5) with 0.01 N precision. Before placing the microfibers in between the clamps of the Alluris, they were electrically insulated by 170 µm thick PET foils. For all electromechanical tests, the microfibers were stretched at a fixed rate of 100 mm min^{-1} (or an equivalent of 8.3% s^{-1}), unless otherwise specified. The DC electrical resistance measurements of microfibers were carried out by a Keithley 2612B source measure unit, under a source voltage of 50 mV.

Li-ion cell Assembly: Cell assembly was performed with commercially available electrodes. The cell contains 20 double-sided cathodes and 21 double-sided anodes. Cathodes consist of $LiNi_{1/3}Mn_{1/3}Co_{1/3}O_2$ (NMC 111) with 94 wt.% active material and are 135 mm × 208 mm in size. Anodes, which consist of graphite, were 139 mm × 212 mm in size, and 143 mm × 216 mm ceramic-coated PET separators were used. Electrodes and separators were dried under reduced pressure for 24 h at 130 °C and 180 °C, respectively. The cell was filled with 80.0 mL LP30 as electrolyte and sealed afterward under reduced pressure. The cell was then stored overnight at 40 °C and has a theoretical capacity of 20 Ah.

Li-ion cell Formation: Initial charging after cell assembly was performed with a constant current (CC) at C/10 and a subsequent constant voltage (CV) to 4.2 V until the current dropped below C/20. Afterward, the cell experienced two cycles at C/2, where charging was again performed using a CC-CV mode (until I < C/20). All electrochemical cell-cycling tests were performed with BasyTec HPS LAB at 26 °C ± 1 °C.

Thickness Measurements of the Li-ion Cell: The thicknesses of the Li-ion cell at different locations were measured using a Heidenhain-Metro MT12B, at 0% SOC and 100% SOC, a report of which is presented in Table S5 (Supporting Information). These thickness measurements were done in the absence of any external pressure or constraints to the pouch cell.

Preparation of Microfiber Strain Sensor Array for Li-ion Cell Expansion Monitoring: Freestanding microfibers were used after they were dried under vacuum at room temperature. For the self-fabricated Li-ion cell, an active sensing length of 7.3 mm was required. Therefore, the ≈2 m long microfiber was cut into 15 mm pieces, then using a silver lacquer each fiber was attached at the sides of the setup to the pre-attached copper tape. Then the contacts were dried at room temperature for 10 min. After microfiber attachments to the setup, to ensure minimal residual strain in the microfibers, before cell thickness monitoring, the setup was held as prepared overnight.

Li-ion cell Expansion Monitoring: For the cell thickness change monitoring, the cell experienced initial discharge at a 1 C rate, followed by four cycles in the voltage window of 3–4.2 V using a 1 C rate with CC-CV (I < C/10) in charge and a 1 C rate with CC in the discharge direction. Afterward, the cell was charged to a nominal voltage of 3.7 V. All electrochemical measurements were performed at 26 °C±1 °C. The reference for the thickness changes was obtained by the Keyence GT2-H12 displacement gauge with a 2 µm accuracy and 0.5 µm resolution. Keyence was installed at the center of the middle plate. As the Li-ion cell was undergoing charge- and discharge cycles, the real-time thickness change reference data was obtained with 1 Hz frequency by Keyence GT-Monitor 2 Test version software. Simultaneously, the resistance changes of the seven microfiber sensors were obtained by Keysight LXI Data Acquisition/Switch Unit (34972A) while a DC voltage of 50 mV was applied to the microfiber and their DC resistance was measured with 1 Hz frequency. The $\Delta R/R_0$ data of the microfiber sensor obtained by the Keysight source measure unit was then correlated to the reference z-direction displacement data of the Keyence displacement sensor.

Supporting Information

Supporting Information is available from the Wiley Online Library or from the author.

**ADVANCED
SCIENCE NEWS**

www.advancedsciencenews.com

**ADVANCED
MATERIALS**

www.advmat.de

Conflict of Interest

The authors declare no conflict of interest.

Author Contributions

P.N. developed the idea and designed the microfibers. P.N. designed the electromechanical experiments of this study. J.Z. provided the dispensing pump for the wet spinning of the microfibers. P.N. and R.B. analyzed the SEM images. P.N. performed the strain tests. P.N., R.B., C.M., J.Z., G.H.S., and U.L. analyzed the results of electromechanical tests. P.N. and C.M. developed the battery thickness monitoring idea. P.N., C.M., J.A.H., and G.H.S. discussed the battery experiments. P.N. designed and prepared the battery thickness monitoring setup. P.N., C.S., and A.S. designed the battery thickness monitoring experiments. P.N., C.S., and A.S. concluded the discussion of the battery thickness monitoring results. P.N., G.H.S., and U.L. concluded the discussion of the results. U.L. supervised the project. All authors discussed the results and contributed to the manuscript writing.

Data Availability Statement

The data that support the findings of this study are available from the corresponding author upon reasonable request.

Keywords

[1] L. K. Willenberg, P. Dechent, G. Fuchs, D. U. Sauer, E. Figgemeier, *Sustainability* **2020**, *12*, 557.

[2] A. J. Louli, L. D. Ellis, J. R. Dahn, *Joule* **2019**, *3*, 745.

[3] P. Mohtat, S. Lee, J. B. Siegel, A. G. Stefanopoulou, *J. Electrochem. Soc.* **2021**, *168*, 100520.

[4] C. P. Grey, J. M. Tarascon, *Nat. Mater.* **2016**, *16*, 45.

[5] P. Mohtat, S. Lee, J. B. Siegel, A. G. Stefanopoulou, *J. Power Sourc.* **2019**, *427*, 101.

[6] J. B. Siegel, A. G. Stefanopoulou, P. Hagans, Y. Ding, D. Gorsich, *J. Electrochem. Soc.* **2013**, *160*, A1031.

[7] X. Yu, Z. Feng, Y. Ren, D. Henn, Z. Wu, K. An, B. Wu, C. Fau, C. Li, S. J. Harris, *J. Electrochem. Soc.* **2018**, *165*, A1578.

[8] J. Hemmerling, J. Guhathakurta, F. Dettinger, A. Fill, K. P. Birke, *Batteries* **2021**, *7*, 61.

[9] A. Li, J. L. Hempel, M. P. Balogh, Y.-T. Cheng, A. I. Taub, *J. Electrochem. Soc.* **2023**, *170*, 010533.

[10] P. K. Leung, C. Moreno, I. Masters, S. Hazra, B. Conde, M. R. Mohamed, R. J. Dashwood, R. Bhagat, *J. Power Sourc.* **2014**, *271*, 82.

[11] J. Luo, C. Y. Dai, Z. Wang, K. Liu, W. G. Mao, D. N. Fang, X. Chen, *Measurement* **2016**, *94*, 759.

[12] X. M. Liu, C. B. Arnold, *J. Electrochem. Soc.* **2016**, *163*, A2501.

[13] J. Cannarella, C. B. Arnold, *J. Power Sourc.* **2014**, *269*, 7.

[14] A. J. Louli, J. Li, S. Trussler, C. R. Fell, J. R. Dahn, *J. Electrochem. Soc.* **2017**, *164*, A2689.

[15] S. L. Glazier, J. Li, A. J. Louli, J. P. Allen, J. R. Dahn, *J. Electrochem. Soc.* **2017**, *164*, A3545.

[16] K.-Y. Oh, B. I. Epureanu, *J. Power Sourc.* **2016**, *303*, 86.

[17] A. G. Hsieh, S. Bhadra, B. J. Hertzberg, P. J. Gjeltema, A. Goy, J. W. Fleischer, D. A. Steingart, *Energy Environ. Sci.* **2015**, *8*, 1569.

[18] P. Ladpli, F. Kopsaftopoulos, F.-K. Chang, *J. Power Sourc.* **2018**, *384*, 342.

[19] A. Ganguli, B. Saha, A. Raghavan, P. Kiesel, K. Arakaki, A. Schuh, J. Schwartz, A. Hegyi, L. W. Sommer, A. Lochbaum, S. Sahu, M. Alamgir, *J. Power Sourc.* **2017**, *341*, 474.

[20] J. Peng, X. Zhou, S. Jia, Y. Jin, S. Xu, J. Chen, *J. Power Sourc.* **2019**, *433*, 226692.

[21] L. Albero Blanquer, F. Marchini, J. R. Seitz, N. Daher, F. Bétermier, J. Huang, C. Gervillié, J.-M. Tarascon, *Nat. Commun.* **2022**, *13*, 1153.

[22] G. Han, J. Yan, Z. Guo, D. Greenwood, J. Marco, Y. Yu, *Renew Sustain Energy Rev* **2021**, *150*, 111514.

[23] Y.-D. Su, Y. Preger, H. Burroughs, C. Sun, P. R. Ohodnicki, *Sensors* **2021**, *21*, 1397.

[24] K. Kim, B. Kim, C. H. Lee, *Adv. Mater.* **2020**, *32*, 1902051.

[25] L. Duan, D. R. D'hooge, L. Cardon, *Prog. Mater. Sci.* **2020**, *114*, 100617.

[26] M. Baumgartner, F. Hartmann, M. Drack, D. Preninger, D. Wirthl, R. Gerstmayr, L. Lehner, G. Mao, R. Pruckner, S. Demchyshyn, L. Reiter, M. Strobel, T. Stockinger, D. Schiller, S. Kimeswenger, F. Greibich, G. Buchberger, E. Bradt, S. Hild, S. Bauer, M. Kaltenbrunner, *Nat. Mater.* **2020**, *19*, 1102.

[27] H. Souri, H. Banerjee, A. Jusufi, N. Radacsi, A. A. Stokes, I. Park, M. Sitti, M. Amjadi, *Adv. Intell. Syst.* **2020**, *2*, 2000039.

[28] C. Tan, Z. Dong, Y. Li, H. Zhao, X. Huang, Z. Zhou, J.-W. Jiang, Y.-Z. Long, P. Jiang, T.-Y. Zhang, B. Sun, *Nat. Commun.* **2020**, *11*, 3530.

[29] A. Fakharuddin, H. Li, F. Di Giacomo, T. Zhang, N. Gasparini, A. Y. Elezzabi, A. Mohanty, A. Ramadoss, J. Ling, A. Soultati, M. Tountas, L. Schmidt-Mende, P. Argitis, R. Jose, M. K. Nazeeruddin, *Vasilopoulou Adv. Energy Mater.* **2021**, *11*, 2101443.

[30] X. Wu, Y. Han, X. Zhang, C. Lu, *ACS Appl. Mater. Interfaces* **2016**, *8*, 9936.

[31] G.-J. Zhu, P.-G. Ren, H. Guo, Y.-L. Jin, D.-X. Yan, Z.-M. Li, *ACS Appl. Mater. Interf.* **2019**, *11*, 23649.

[32] S. Lee, S. Shin, S. Lee, J. Seo, J. Lee, S. Son, H. J. Cho, H. Algadi, S. Al-Sayari, D. E. Kim, T. Lee, *Adv. Funct. Mater.* **2015**, *25*, 3114.

[33] S. Chen, Y. Wei, S. Wei, Y. Lin, L. Liu, *ACS Appl. Mater. Interfaces* **2016**, *8*, 25563.

[34] Z. Liu, D. Qi, G. Hu, H. Wang, Y. Jiang, G. Chen, Y. Luo, X. J. Loh, B. Liedberg, X. Chen, *Adv. Mater.* **2018**, *30*, 1704229.

[35] J. Gao, X. Wang, W. Zhai, H. Liu, G. Zheng, K. Dai, L. Mi, C. Liu, C. Shen, *ACS Appl. Mater. Interf.* **2018**, *10*, 34592.

[36] L. Lu, Y. Zhou, J. Pan, T. Chen, Y. Hu, G. Zheng, K. Dai, C. Liu, C. Shen, X. Sun, H. Peng, *ACS Appl. Mater. Interf.* **2019**, *11*, 4345.

[37] X. Qu, Y. Wu, P. Ji, B. Wang, Q. Liang, Z. Han, J. Li, Z. Wu, S. Chen, G. Zhang, H. Wang, *ACS Appl. Mater. Interf.* **2022**, *14*, 29167.

[38] T. Huang, P. He, R. Wang, S. Yang, J. Sun, X. Xie, G. Ding, *Adv. Funct. Mater.* **2019**, *29*, 1903732.

[39] C. M. Hansen, *Hansen Solubility Parameters: A User's Handbook, Second Edition*, CRC Press, Boca Raton, FL, USA **2007**.

[40] J. Camacho, E. Díez, I. Díaz, G. Ovejero, *Polym. Int.* **2017**, *66*, 1013.

[41] D. R. Paul, *J. Appl. Polym. Sci.* **1968**, *12*, 383.

[42] X. Sun, X. Wang, F. Sun, M. Tian, L. Qu, P. Perry, H. Owens, X. Liu, *Adv. Mater.* **2021**, *33*, 2105174.

[43] B. Fang, J. Yan, D. Chang, J. Piao, K. M. Ma, Q. Gu, P. Gao, Y. Chai, X. Tao, *Nat. Commun.* **2022**, *13*, 2101.

[44] J. Zhou, X. Xu, Y. Xin, G. Lubineau, *Adv. Funct. Mater.* **2018**, *28*, 1705591.

[45] L. Kou, T. Huang, B. Zheng, Y. Han, X. Zhao, K. Gopalsamy, H. Sun, C. Gao, *Nat. Commun.* **2014**, *5*, 3754.

[46] O. Mysiukiewicz, B. Gospodarek, P. Ławniczak, T. Sterzyński, *Adv. Polym. Technol.* **2018**, *37*, 3542.

[47] K. Wang, Q. Deng, *Polymers (Basel)* **2019**, *11*, 1055.

[48] G. Acik, M. Kamaci, C. E. Cansoy, *Colloid Polym. Sci.* **2018**, *296*, 1759.

[49] J. Wang, X. Zhang, L. Jiang, J. Qiao, *Prog. Polym. Sci.* **2019**, *98*, 101160.

[50] C. S. Boland, *ACS Nano* **2019**, *13*, 13627.

[51] F. Bueche, *J. Appl. Polym. Sci.* **1960**, *4*, 107.

[52] M. Amjadi, K.-U. Kyung, I. Park, M. Sitti, *Adv. Funct. Mater.* **2016**, *26*, 1678.

[53] M. A. O'Mara, S. P. Ogilvie, M. J. Large, A. Amorim Graf, A. C. Sehnal, P. J. Lynch, J. P. Salvage, I. Jurewicz, A. A. K. King, A. B. Dalton, *Adv. Funct. Mater.* **2020**, *30*, 2002433.

[54] C. S. Boland, U. Khan, G. Ryan, S. Barwich, R. Charifou, A. Harvey, C. Backes, Z. Li, M. S. Ferreira, M. E. Möbius, R. J. Young, J. N. Coleman, *Science* **2016**, *354*, 1257.

[55] C. S. Boland, *ACS Appl. Nano Mater.* **2020**, *3*, 11240.

[56] O. A. Araromi, M. A. Graule, K. L. Dorsey, S. Castellanos, J. R. Foster, W.-H. Hsu, A. E. Passy, J. J. Vlassak, J. C. Weaver, C. J. Walsh, R. J. Wood, *Nature* **2020**, *587*, 219.

[57] W. Li, Y. Zhou, Y. Wang, L. Jiang, J. Ma, S. Chen, F.-L. Zhou, *Adv. Electron. Mater.* **2021**, *7*, 2000865.

[58] Y. Cheng, R. Wang, J. Sun, L. Gao, *Adv. Mater.* **2015**, *27*, 7365.

[59] J. Zhou, X. Xu, H. Yu, G. Lubineau, *Nanoscale* **2017**, *9*, 604.

[60] H. Cho, S. Mayer, E. Pöselt, M. Susoff, P. J. in 't Veld, G. C. Rutledge, M. C. Boyce, *Polymer (Guildf)* **2017**, *128*, 87.

[61] C. S. Boland, *ACS Appl Polym Mater* **2020**, *2*, 3474.

[62] K.-Y. Oh, J. B. Siegel, L. Secondo, S. U. Kim, N. A. Samad, J. Qin, D. Anderson, K. Garikipati, A. Knobloch, B. I. Epureanu, C. W. Monroe, A. Stefanopoulou, *J. Power Sourc.* **2014**, *267*, 197.

[63] P. Vorwerk, S.-K. Hahn, C. Daniel, U. Krause, K. Keutel, *Batteries* **2022**, *8*, 42.

[64] B. Rieger, S. Schlueter, S. V. Erhard, J. Schmalz, G. Reinhart, A. Jossen, *J. Energy Stor.* **2016**, *6*, 213.

[65] X. Zhang, J. He, J. Zhou, H. Chen, W. Song, D. Fang, *Sci China Technol Sci* **2021**, *64*, 83.

2212189 (11 of 11)